Materials Transactions, Vol. 65, No. 7 (2024) pp. 773 to 779

Effect of Strain Rate on the Extremely Low-Cycle Fatigue of Fe-15Mn-10Cr-8Ni-4Si Bidirectional-TRIP Steel*1

Fumiyoshi Yoshinaka*2, Nobuo Nagashima and Takahiro Sawaguchi

National Institute for Materials Science, Tsukuba 305-0047, Japan

Extremely low cycle fatigue tests, up to a total axial strain amplitude of 10%, were conducted on Fe-15Mn-10Cr-8Ni-4Si bidirectional transformation-induced plasticity (B-TRIP) steel. The fatigue life was approximately five times longer than that of SUS316 when the total strain amplitude was 4% or higher. The improved fatigue life of Fe-15Mn-10Cr-8Ni-4Si was attributed to reversible bidirectional $\gamma \leftrightarrow \varepsilon$ transformation during fatigue deformation, which might mitigate fatigue damage. In contrast, the fatigue life tended to decrease with increasing strain rate when the strain rate was varied from 0.1 to 2.5%/s with a total strain amplitude of 10%. Fractography revealed that the fracture surface varied significantly with strain rate. At low strain rates, crystallographic fracture surfaces characterized by facets and secondary cracks were observed, whereas these features were not observed at high strain rates. Electron backscatter diffraction measurements of the postmortem microstructure showed that frequent ε-martensite formation occurred at low strain rates, whereas martensitic transformation was suppressed at high strain rates. The change in the specimen surface temperature was evaluated in terms of the Gibbs free energy difference between γ-austenite and ε-martensite (i.e., $\Delta G^{\gamma\to\varepsilon}$), and the effect of strain rate on the extremely low cycle fatigue was discussed from the viewpoint of the deformation mechanism. At a low strain rate, the condition for B-TRIP to work effectively, that is, $\Delta G^{\gamma\to\varepsilon}$ is negative but close to zero, was maintained over the entire life span. At a high strain rate, the deformation mechanism changed to one in which γ-austenite was dominant because of the increase in $\Delta G^{\gamma\to\varepsilon}$ caused by self-heating; the fatigue damage mitigation mechanism provided by B-TRIP was less likely to occur at high strain rates, which reduced the fatigue life. [doi:10.2320/matertrans.MT-Z2024002]

(Received February 15, 2024; Accepted April 16, 2024; Published April 26, 2024)

Keywords: *fatigue, fracture surface, extremely low cycle fatigue, microstructure, martensitic transformation, seismic damper*

1. Introduction

A vibration control structure is one in which seismic dampers act as energy-absorbing components to reduce the shaking of the building and minimize damage to the main structural members such as columns and beams. There are several types of seismic dampers, including steel, oil, and rubber dampers. Steel dampers absorb seismic energy input to a building by converting it to heat through elastoplastic deformation. Steel dampers offer advantages over other types of dampers because of their low cost and ability to add stiffness to buildings. However, since their operation principle involves cyclic elastoplastic deformation, they exhibit low cycle fatigue. Therefore, their design should be based on the limited life design concept. In other words, the product life of a steel damper depends on the fatigue durability against low cycle fatigue (or plastic fatigue) of the steel used as the core material.

Japan regularly experiences major earthquakes, such as the Great East Japan Earthquake in 2011, the Kumamoto Earthquake in 2016, the Hokkaido Eastern Iburi Earthquake in 2018, and the Noto Earthquake in 2024. Additionally, the Nankai Trough Earthquake is predicted to occur with a high probability. Therefore, earthquake preparedness is extremely important. Recently, the problem of long-term long-period ground motion has attracted much attention. Structures that have a long natural period, such as high-rise buildings, may resonate with the long-period component of ground motion, causing long-lasting strong shaking. Conventional steel dampers cannot cope with long-term long-period ground motion because the plastic fatigue life of conventional steel is too short to endure the severe cyclic deformation.

In general, the type of steel is unlikely to significantly impact plastic fatigue life [1]. However, our previous work developed Fe-15Mn-10Cr-8Ni-4Si alloy, which exhibits a long plastic fatigue life because of its deformation reversibility [2–5]. This Fe-15Mn-10Cr-8Ni-4Si alloy has been used as a seismic damper in some structures in Japan. The deformation mechanism of this alloy is characterized by reversible bidirectional transformation between the face-centered-cubic structure, γ-austenite, which is an initial microstructure, and the hexagonal-closed-packed structure, ε-martensite; this transformation is called $\gamma \leftrightarrow \varepsilon$ transformation [5]. Extended plastic fatigue life may be attributed to fatigue damage mitigation resulting from high deformation reversibility.

In practical applications of Fe-15Mn-10Cr-8Ni-4Si alloy as a seismic damper, the expected deformation, specifically, the total axial strain amplitude, is up to 1% during shaking caused by L2 ground motion under extremely rare earthquakes. When a joint part is subjected to fatigue deformation, it is necessary to consider the occurrence of significant strain concentration, and when a damper shape such as a U shape [6] or a lens shape [7] is used, it is necessary to assume that large deformation will occur repeatedly. In addition, it is required to consider L3 ground motion under extreme earthquakes that exceed the conventional assumption of L2 ground motion. Therefore, it is crucial to understand the extremely low cycle fatigue property of Fe-15Mn-10Cr-8Ni-4Si alloy to guarantee its integrity when used as a seismic damper.

Our previous work conducted extremely low cycle fatigue tests on the alloy involving a maximum total strain amplitude of 10%, converted to the axial direction from the radial direction [8]. The present work conducted fatigue tests at a

---

[*1] This Paper was Originally Published in Japanese in J. Japan Inst. Met. Mater. **72** (2023) 858–865. The captions of Table 1 and Figs. 1, 6, and 7 are slightly modified.

[*2] Corresponding author, E-mail: YOSHINAKA.Fumiyoshi@nims.go.jp

total axial strain amplitude of 10% with different strain rates. The effect of strain rate on the extremely low cycle fatigue of Fe-15Mn-10Cr-8Ni-4Si alloy was determined based on fracture surface observation and microstructural analysis.

2. Experimental Procedure

An Fe-15Mn-10Cr-8Ni-4Si (mass%) alloy was used in this study. The microstructure after heat treatment at 1273 K for 1 h followed by water quenching was γ-austenite with an average grain size of 95 µm.

A radial strain-controlled fatigue test was conducted using a 50 kN servo-hydraulic fatigue testing machine. Triangular waves were applied to the specimen at a strain ratio of −1, total radial strain amplitudes ($\varepsilon_{\mathrm{td,a}}$) of 2, 3, 4, and 5%, and an axial strain rate of 0.5%/s (hereafter, these tests are referred to as the single strain rate tests). In addition, tests at $\varepsilon_{\mathrm{td,a}} = 5\%$ were performed with axial strain rates of 0.1, 0.5, and 2.5%/s to study the effect of strain rate (hereafter, these tests are referred to as the multiple strain rate tests). An hourglass-shaped specimen with a minimum diameter of 6 mm was subjected to the single strain rate tests, and an hourglass-shaped specimen with a minimum diameter of 8 mm was subjected to the multiple strain rate tests. Radial strain was monitored to control the test using an extensometer attached to the minimum diameter part along the radial direction. The temperature at the specimen surface was measured during the fatigue test using a Type T thermocouple wire. The measurement point was approximately centered in the specimen. The radial strain $\varepsilon_{\mathrm{td}}$ was converted to axial strain $\varepsilon_{\mathrm{tl}}$ by the following equation:

$$\varepsilon_{\mathrm{tl,a}} = (\sigma_{\mathrm{a}}/E)(1 - 2\nu) + 2\varepsilon_{\mathrm{pd,a}} \quad (1)$$

where $\varepsilon_{\mathrm{tl,a}}$, σ_{a}, E, and ν are the total axial strain amplitude, stress amplitude, Young's modulus (189 GPa), and Poisson's ratio (0.27), respectively. The total strain amplitude can be written as the summation of the elastic and plastic components, and the first term on the right-hand side of eq. (1) shows the elastic component. The second term represents the plastic component, where $\varepsilon_{\mathrm{pd,a}}$ was measured as half of the distance between the x-axis (strain axis) intercepts on the hysteresis loop, i.e., half of the plastic radial strain range. Hereafter, unless otherwise noted, strain amplitude and strain rate refer to axial values.

Fractography was performed using a field-emission scanning electron microscope (FE-SEM) (Thermo Fisher, Scios2), and Thermo Scientific MAPS software was used to automatically capture the overall fracture surface.

The fracture surface was cut parallel to the direction of the load axis using a precision cutting machine to expose the longitudinal section for analysis of the microstructure beneath the fracture surface. The cutting positions were approximately through the fracture origin. The sample was wet polished with #180–#1200 waterproof abrasive paper, followed by intermediate polishing with 9, 3, and 1 µm diamond abrasives, and then finished with colloidal silica for a mirror finish. Observations were performed using an FE-SEM (JEOL, JSM-7900F), and electron backscatter diffraction (EBSD) measurements were conducted using a detector (DVC5, TSL) equipped with the FE-SEM. The EBSD data were analyzed using OIM Analysis v8 software (EDAX).

3. Results

Figure 1 shows the ε-N curve, representing the relationship between the total strain amplitude $\varepsilon_{\mathrm{tl}}$, a and the fatigue life N_{f} obtained by the single strain rate tests (0.5%/s) [8]. The results of the axial strain-controlled fatigue tests at total strain amplitudes of 0.25%–2% obtained with a strain rate of 0.4%/s in the previous work (○) [3] and the results of the multiple strain rate tests in the present work (◆) are plotted in the figure along with the results of the single strain rate tests (●). Additionally, the results of SUS316 obtained by Kamaya (△) [9] are presented in the figure for comparison. The Fe-15Mn-10Cr-8Ni-4Si alloy exhibited an extended fatigue life compared to SUS316. In the regime of extremely low cycle fatigue, the fatigue life of Fe-15Mn-10Cr-8Ni-4Si alloy was approximately five times longer than that of SUS316, and it was found to be 28 cycles at $\varepsilon_{\mathrm{tl,a}} = 10\%$.

Table 1 lists the fatigue lives at $\varepsilon_{\mathrm{tl,a}} = 10\%$ under strain rates of 0.1, 0.5, and 2.5%/s obtained by the multiple strain rate tests. As shown in the table, fatigue life decreased with increasing strain rate. The fatigue life of SUS316 at $\varepsilon_{\mathrm{tl,a}} = 10\%$, estimated by extrapolating the results shown in Fig. 1, was $N_{\mathrm{f}} = 9$ cycles. Thus, although the fatigue life of Fe-15Mn-10Cr-8Ni-4Si alloy decreased with increasing strain rate, it remained superior (approximately two times longer) compared to that of conventional steel.

Figure 2 shows the relationship between N and the maximum stress $\sigma_{\max}$ from the multiple strain rate tests.

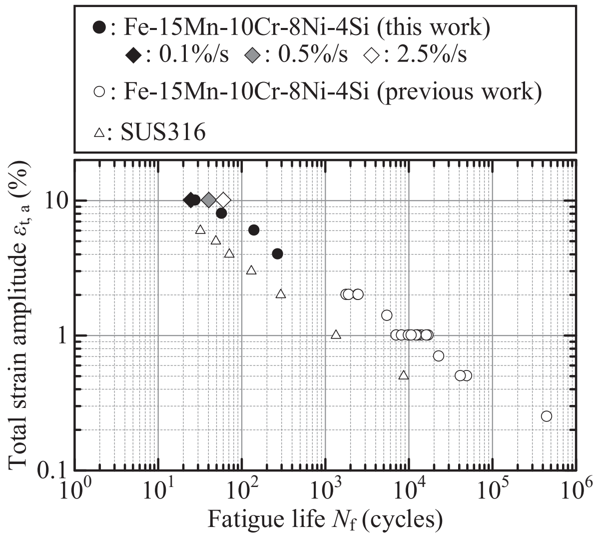

Fig. 1 Relationship between the total strain amplitude and fatigue life.

Table 1 Results of fatigue tests at a total axial strain amplitude of 10% and different strain rates.

Axial strain rate [%/s]	Fatigue life (cycles)	Maximum stress at $N_{\mathrm{f}}/2$ [MPa]
0.1	61	745
0.5	41	802
2.5	25	840

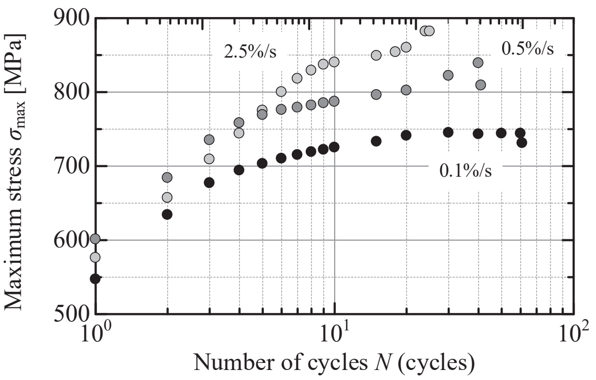

Fig. 2 Relationship between the number of cycles N and the maximum stress $\sigma_{\max}$ at total axial strain amplitude of 10%.

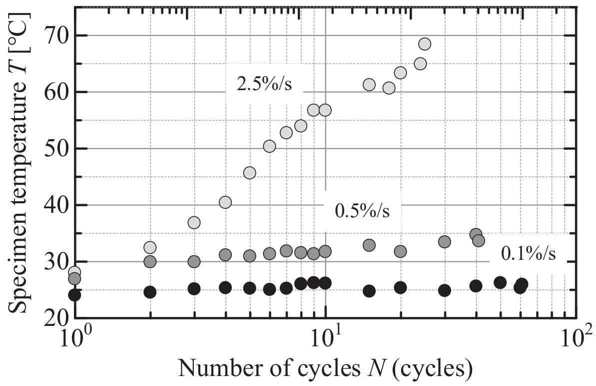

Fig. 3 Relationship between the number of cycles N and the specimen temperature T during the fatigue test at a total axial strain amplitude of 10%.

Remarkable hardening occurred during the initial part of the fatigue tests at all strain rates. In the test at 0.1%/s, the hardening became saturated with additional cyclic loadings, whereas in the tests at 0.5 and 2.5%/s, the hardening continued until fatigue fractures occurred. Significant hardening was observed, particularly at 2.5%/s. The maximum stress at half-life $N_f/2$ increased with the strain rate, as shown in Table 1.

Figure 3 shows the specimen temperature during the fatigue tests. In the test at 0.1%/s, the temperature was almost stable at room temperature, whereas in the tests at 0.5 and 2.5%/s, the temperature increased with cyclic loadings. Significant self-heating was observed, particularly at 2.5%/s. In the following section, the mechanism of extremely low cycle fatigue of Fe-15Mn-10Cr-8Ni-4Si alloy is investigated by analyzing the fatigue fracture and deformation microstructure obtained from the multiple strain rate tests.

Figures 4(a)–(c) show the overall fracture surfaces. The fracture origin was on the specimen surface regardless of the strain rate. Figures 4(d) and (e) show the magnified view of the region formed by fatigue crack growth in the tests at

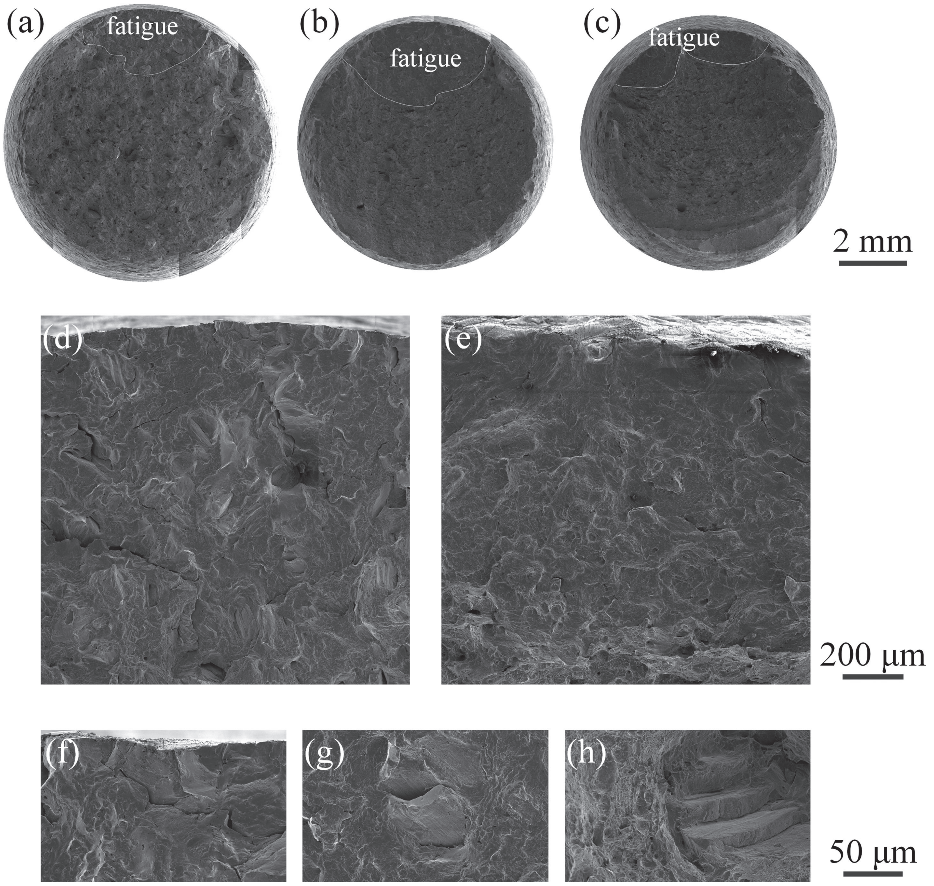

Fig. 4 Fracture surface. (a)–(c) Overall fracture surface obtained with strain rates of 0.1%/s, 0.5%/s, and 2.5%/s. (d)–(e) Fatigue crack growth region in (a) and (c). (f)–(h) Magnified view of the fracture surface at the fracture origin, the fatigue crack growth region, and the fast fracture region in (a).

0.1%/s and 2.5%/s. The fracture surface obtained at 0.1%/s had an angular crystallographic morphology, frequently displaying facets and secondary cracks. In contrast, the fracture surface obtained at 2.5%/s had a rounded morphology without facets. Figures 4(f)–(h) present examples of the crystallographic morphologies observed on the fracture surface obtained at 0.1%/s. Facets and secondary cracks were observed in the origin site and the fatigue crack growth region. Secondary cracks were often found at the edges of facets. In the final fracture region after fatigue crack growth, dimples coexisting with facets were observed. In the case of 2.5%/s strain rate, only dimples were observed in the final fracture region. The fatigue fracture surface significantly changed with varying strain rate, as shown in Fig. 4, and a crystallographic fracture surface characterized by facets and secondary cracks was formed when the strain rate was low.

Figures 5(a) and (b) show the SEM images of the longitudinal section obtained at strain rates of 0.1%/s and 2.5%/s, respectively. The macrographic crack growth direction was oriented from right to left. The blue open arrows, green blank closed arrows, and red solid closed arrows point at secondary cracks from the main crack, surface cracks, and internal cracks, respectively. Although the fracture origin was on the specimen surface, as shown in Fig. 4, internal cracks were also present on the longitudinal sections. The number of cracks on the longitudinal section varied significantly depending on the strain rate, with many cracks observed when the strain rate was 0.1%/s.

EBSD analysis was conducted on longitudinal sections. The measurement areas located beneath the fatigue crack growth regime are represented by the dashed rectangles in Figs. 5(a) and (b). The size of the measurement area was 800 µm × 800 µm, and the measurement step was 1 µm. The EBSD phase and grain boundary maps are shown in Figs. 6(a) and (b) for 0.1%/s and Figs. 6(c) and (d) for 2.5%/s. The figures exclude measurement points with a confidential index value less than 0.1. The phase maps are superimposed on the image quality maps. A significant amount of ε-martensite was formed when the strain rate was 0.1%/s, as shown in Fig. 6(a), and the retained γ-austenite locally existed. In addition, limited amounts of α′-martensite were detected. As shown in Fig. 6(c), the deformation microstructure at 2.5%/s consisted only of γ-austenite. Deformation twinning was only found at 2.5%/s, as shown in the grain boundary maps. Deformation microstructure varied with strain rate. At low strain rates, the ε-martensitic transformation occurred frequently, whereas at high strain rates, the transformation was suppressed, and the deformation mechanism changed to one in which γ-austenite was dominant.

4. Discussion

Fe-15Mn-10Cr-8Ni-4Si alloy had an extended fatigue life even at strain levels that cause conventional steels to exhibit extremely low cycle fatigue, as shown in Fig. 1. The alloy underwent bidirectional γ ↔ ε transformation as a plastic deformation mechanism, referred to as B-TRIP [10–13]. High deformation reversibility can improve fatigue life [14–16]. Fe-15Mn-10Cr-8Ni-4Si alloy possesses high deformation reversibility in the form of bidirectional transformation, resulting in extended fatigue life. Although its deformation

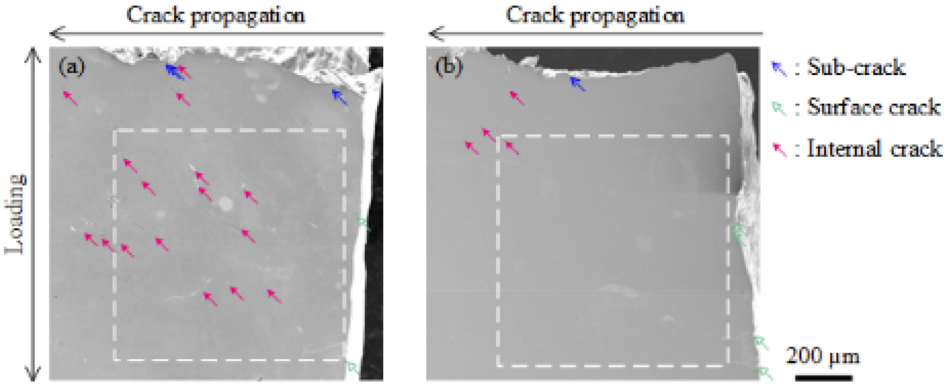

Fig. 5 Longitudinal section at the fatigue crack propagation regime: strain rate of (a) 0.1%/s and (b) 2.5%/s.

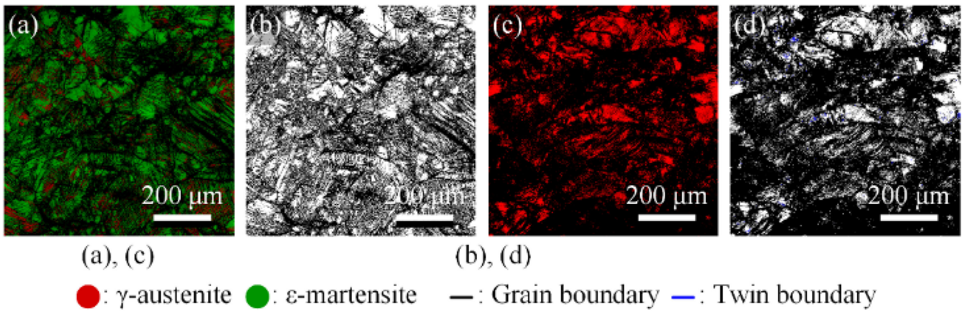

Fig. 6 Electron backscattering diffraction maps of the postmortem microstructure obtained from the region shown in Fig. 4: (a) phase and (b) grain boundary maps for strain rate of 0.1%/s; (c) phase and (d) grain boundary maps for a strain rate of 2.5%/s.

reversibility decreases with increasing strain, Fe-15Mn-10Cr-8Ni-4Si alloy still exhibits superior fatigue life compared to conventional steel at a high strain level [15]. Therefore, the fatigue improvement mechanism via B-TRIP may be effective in the extremely low cycle fatigue regime.

The fatigue life and cyclic hardening behavior of Fe-15Mn-10Cr-8Ni-4Si alloy varied with strain rate, as shown in Table 1, respectively. Furthermore, the fatigue fracture surface and deformation microstructure were dependent on the strain rate. As shown in Fig. 4, the fatigue fracture surfaces obtained at a low strain rate (resulting in longer fatigue life) often displayed facets and secondary cracks, whereas these features were not observed in the fracture surface obtained at a high strain rate (resulting in shorter fatigue life). In terms of the fatigue deformation microstructure, large amounts of ε-martensite were detected at a low strain rate, whereas ε-martensitic transformation was significantly suppressed at a high strain rate. Previous work on the fracture surface of Fe-33Mn-6Si alloy reported that it had a crystallographic appearance consisting mainly of facets with frequent secondary cracks [17]. This may be attributed to the high probability of ε-martensitic transformation due to its low stacking fault energy (SFE) Γ_{SFE}. Therefore, the crystallographic fracture surface observed in Fe-15Mn-10Cr-8Ni-4Si alloy at a low strain rate may also be attributed to ε-martensite. The absence of facets on the fracture surface at a high strain rate can be explained by the significant suppression of ε-martensite.

Austenitic steels, including Fe-15Mn-10Cr-8Ni-4Si alloy, exhibit different plastic deformation mechanisms depending on the SFE [18].

$$\Gamma_{\mathrm{SFE}} = 2\rho\Delta G^{\gamma\to\varepsilon} + 2\sigma^{\gamma/\varepsilon} \tag{2}$$

where the molar surface fraction on the γ plane is ρ, the Gibbs free energy difference between γ-austenite and ε-martensite is $\Delta G^{\gamma\to\varepsilon}$, and the surface entropy interfacial surface energy between the γ- and ε-phases is $\sigma^{\gamma/\varepsilon}$. A detailed description of the Γ_{SFE} and $\Delta G^{\gamma\to\varepsilon}$ is presented in the previous paper [19]. The plastic deformation mechanism changes from stress-assisted ε-martensitic transformation to strain-induced ε-martensitic transformation, deformation γ-twinning, and γ-slip with increasing SFE. For instance, Fe-33Mn-6Si alloy can readily undergo ε-martensitic transformation due to its low SFE.

Previous work on the low cycle fatigue behavior of Fe-Mn-Al-Si alloys with systematically varied SFE demonstrated that the cyclic hardening behavior varied accordingly [20]. Significant cyclic hardening occurred in all alloys. However, the lower SFE alloys exhibited saturation in hardening with the progress of the fatigue cycle, whereas the higher SFE alloys showed noticeable secondary hardening. A previous study proposed that a higher SFE, which makes cross slip more likely to occur, triggers an interaction with the lattice dislocation, resulting in secondary hardening. As shown in Fig. 2, Fe-15Mn-10Cr-8Ni-4Si alloy exhibited saturation in the hardening when it had lower SFE, whereas it showed secondary hardening when it had higher SFE. The high strain rate test demonstrated significant self-heating, leading to an increase in SFE. In general, a high strain rate causes an increase in the deforming stress due to enhanced viscous resistance to dislocation motion. However, the increase in SFE due to self-heating may play a role in the strain rate dependence of the cyclic hardening behavior in the Fe-15Mn-10Cr-8Ni-4Si alloy.

In our previous work, the occurrence conditions for B-TRIP were expressed as $\Delta G^{\gamma\to\varepsilon} \leq 0$ ($\Delta G^{\gamma\to\varepsilon}$ is negative and close to zero) [21]. Additionally, the relationship between the plastic deformation mechanism and the fatigue life was characterized by $\Delta G^{\gamma\to\varepsilon}$ [19]. Therefore, in this study, $\Delta G^{\gamma\to\varepsilon}$ was used instead of Γ_{SFE} to discuss the effect of strain rate. The increase in $\Delta G^{\gamma\to\varepsilon}$, which has a positive dependence on temperature, implies an increase in the stability of γ-austenite with respect to ε-martensite. Therefore, the significant strain rate dependence of the fatigue life of Fe-15Mn-10Cr-8Ni-4Si, shown in Table 1, may be attributed to the increase in $\Delta G^{\gamma\to\varepsilon}$ due to self-heating at a higher strain rate. Thus, the specimen temperature shown in Fig. 3 was converted to $\Delta G^{\gamma\to\varepsilon}$, and the change in $\Delta G^{\gamma\to\varepsilon}$ with the number of cycles is shown in Fig. 7. As shown in Figs. 3 and 7, no significant self-heating occurred at a strain rate of 0.1%/s, and the condition of $\Delta G^{\gamma\to\varepsilon} \leq 0$ was satisfied throughout the fatigue life, resulting in enhanced fatigue durability due to B-TRIP. As shown in Fig. 6(a), the postmortem microstructure was mainly occupied by ε-martensite at the strain rate of 0.1%/s. As previously mentioned, Fe-33Mn-6Si alloy can readily undergo ε-martensitic transformation, resulting in a large amount of ε-martensite after fatigue fracture. An extremely low cycle fatigue test has not yet been conducted on Fe-33Mn-6Si alloy, but its fatigue life at a total strain amplitude of less than 2% was not long [17]. Therefore, the ε-martensitic transformation is not likely to contribute to the improvement of fatigue life. The Fe-15Mn-10Cr-8Ni-4Si alloy exhibited enhanced fatigue life due to B-TRIP; however, not all of the ε-martensite formed by the forward transformation (γ → ε transformation) underwent the reverse transformation (ε → γ transformation), and the gradual accumulation of ε-martensite up to the fatigue fracture may have developed the deformation microstructure shown in Fig. 6(a).

As shown in Fig. 5, many cracks were initiated inside the material at a low strain rate. It has been reported that the fracture mode caused by internal cracks due to the static fracture mechanism occurs in the extremely low cycle fatigue in addition to the fracture mode caused by surface cracks

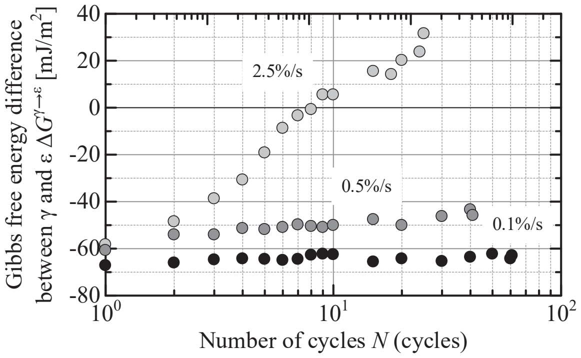

Fig. 7 Relationship between the number of cycles N and the Gibbs free energy difference between γ-austenite and ε-martensite, that is, $\Delta G^{\gamma\to\varepsilon}$, during fatigue test at a total axial strain amplitude of 10%.

according to the general fatigue crack growth law [22]. Koyama *et al.* reported that the formation of ε-martensite triggers the brittle-like crack initiation, resulting in premature fracture in the tensile fracture of high-Mn steel [23]. Therefore, many internal cracks found at the low strain rate despite the extended fatigue life can be attributed to the deformation-induced ε-martensite, which can be the initiation site of the crack due to the static fracture mechanism. However, the Fe-15Mn-10Cr-8Ni-4Si alloy showed surface fracture regardless of the strain rate, and there was no evidence of coalescence with internal cracks initiated independently of the main (surface) crack on the fracture surface, as shown in Fig. 4. Therefore, the fatigue life of this alloy can be evaluated using the fatigue crack growth law for general low cycle fatigue, at least in the range of strain rates investigated in the present work.

At a strain rate of 2.5%/s, the $\Delta G^{\gamma\rightarrow\varepsilon}$ increased and eventually became positive as the test progressed, resulting in the deformation of γ-austenite without the martensitic transformation, as shown in Fig. 6(c). Significant self-heating due to high strain rate, which increased $\Delta G^{\gamma\rightarrow\varepsilon}$, inhibited the bidirectional transformation, resulting in a decrease in fatigue life. However, the M_d point—the upper limit of the temperature at which martensite can be induced by plastic deformation—of Fe-15Mn-10Cr-8Ni-4Si alloy is 100°C [19], and the maximum temperature measured at a strain rate of 2.5%/s (shown in Fig. 3) was lower than the Md point. The measurement point of the specimen temperature was approximately located at the minimum diameter, but it was impossible to place the thermocouple at the exact point at which maximum strain occurred because the extensometer needed to be placed there. Self-heating is expected to be more pronounced in the locations at which large deformations occur, and the temperature at the minimum diameter may have been higher than that shown in Fig. 3. In addition, the fatigue crack is expected to cause further self-heating at its tip [24] thereby increasing SFE. Figure 5 was taken from the lower region of the fracture surface, and as shown in Fig. 6(c), little martensitic transformation occurred at high strain rates, which can be explained by the local heat generation near the crack. A detailed analysis of the local heat generation at the crack propagation zone and the fatigue deformation microstructure around the crack is a subject for future study.

As described in Section 3, the fatigue life of Fe-15Mn-10Cr-8Ni-4Si alloy decreased with increasing strain rate and was 25 cycles, which was more than double that of SUS316, even at the highest strain rate of 2.5%/s. The decrease in fatigue life was due to self-heating, as discussed above. However, the increase in specimen temperature due to self-heating gradually occurred over the entire fatigue life at a high strain rate (Fig. 3), as did the associated increase in $\Delta G^{\gamma\rightarrow\varepsilon}$ (Fig. 7). Therefore, B-TRIP was effective in the early stage of fatigue life, leading to the longer fatigue life compared to general steel at a high strain rate. In addition, it is unrealistic to assume that high-speed large deformations will continue until fatigue fracture during a real-world earthquake. Instead, intermittent deformations are more likely to occur. In this case, even if self-heating occurs because of high-speed large deformations, if sufficient heat removal is achieved, B-TRIP in the subsequent fatigue deformation and the fatigue damage accumulation mechanism might be effective. In other words, the fatigue test under constant high strain rate conducted in the present work is significant because it represents the worst case of fatigue fracture of Fe-15Mn-10Cr-8Ni-4Si alloy. In conclusion, Fe-15Mn-10Cr-8Ni-4Si alloy exhibits excellent fatigue life under large cyclic deformation when the heat generated during deformation is properly controlled. This alloy helps to ensure design margins against extreme earthquakes and has strong potential for application in various types of seismic dampers.

5. Conclusion

Fe-15Mn-10Cr-8Ni-4Si alloy, developed for steel damper exhibits bidirectional $\gamma \leftrightarrow \varepsilon$ transformation (B-TRIP) as a plastic deformation mechanism that mitigates the accumulation of fatigue damage, resulting in approximately five times longer fatigue life compared to SUS316 at a total axial strain amplitude over 4%. However, the fatigue life decreased with increasing strain rate between 0.1%/s and 2.5%/s at a total axial strain amplitude of 10%. The fatigue fracture surface also changed with strain rate; facets and secondary cracks were observed at a low strain rate (longer fatigue life), whereas these features were hardly observed at a high strain rate (shorter fatigue life). EBSD analysis of the deformation microstructure demonstrated that the $\gamma \rightarrow \varepsilon$-martensitic transformation occurred frequently at a low strain rate, whereas the transformation was suppressed at a high strain rate. The specimen temperature measurement revealed that significant self-heating occurred only at a high strain rate of 2.5%/s, indicating that the increase in $\Delta G^{\gamma\rightarrow\varepsilon}$ due to self-heating inhibited B-TRIP, resulting in a decrease in fatigue life at high strain rates. The fact that the Fe-15Mn-10Cr-8Ni-4Si alloy maintained a relatively long fatigue life compared to general steel implies that the fatigue damage mitigation mechanism due to B-TRIP was effective at the early stage of fatigue life when less self-heating had occurred.

Acknowledgments

The authors acknowledge the support of Grants-in-Aid for Early-Career Scientists (19K14853 and 23K13227) and a Grant-in-Aid for Scientific Research (C) (20K04170) from the Japan Society for the Promotion of Science, Japan.

REFERENCES

[1] K. Hatanaka: Cyclic stress-strain response and low-cycle fatigue life in metallic materials, JSME Int. J. Ser. 1 **33** (1990) 13–25.

[2] I. Nikulin, T. Sawaguchi, K. Ogawa and K. Tsuzaki: Effect of γ to ε martensitic transformation on low-cycle fatigue behaviour and fatigue microstructure of Fe–15Mn–10Cr–8Ni–*x*Si austenitic alloys, Acta Mater. **105** (2016) 207–218.

[3] F. Yoshinaka, T. Sawaguchi, I. Nikulin, S. Takamori and N. Nagashima: Improved fatigue life of the newly developed Fe-15Mn-10Cr-8Ni-4Si seismic damping alloy, Procedia Struct. Integr. **19** (2019) 214–223.

[4] F. Yoshinaka, T. Sawaguchi, I. Nikulin and S. Takamori: Fatigue properties and plastically deformed microstructure of Fe-15Mn-10Cr-8Ni-4Si alloy in high-cycle-fatigue regime, Int. J. Fatigue **129** (2019) 105224.

[5] F. Yoshinaka, T. Sawaguchi, S. Takamori and S. Emura: Transformation-induced plasticity via $\gamma \rightarrow \varepsilon \rightarrow \alpha'$ and $\gamma \rightarrow \varepsilon \rightarrow \gamma$ martensitic transformations in Fe–15Mn–10Cr–8Ni–4Si alloy, Mater. Sci. Eng. A **833** (2022) 142583.

[6] Y. Jiao, S. Kishiki, S. Yamada, D. Ene, Y. Konishi, Y. Hoashi and M. Terashima: Low cyclic fatigue and hysteretic behavior of U-shaped steel dampers for seismically isolated buildings under dynamic cyclic loadings, Earthquake Eng. Struct. Dynam. **44** (2015) 1523–1538.

[7] S. Kawase, M. Kubota, N. Yamazaki, M. Hada, M. Morosawa, Y. Ishiwata and Y. Yamasaki: Development of lens shear panel damper using Fe-Mn-Si-based alloy, Tobishima Technical Report **70** (2022) 45–48.

[8] N. Nagashima, F. Yoshinaka and T. Sawaguchi: Study on Extremely-Low-Cycle Fatigue of Fe–15Mn–10Cr–8Ni–4Si Alloy, Mater. Trans. **64** (2023) 548–554.

[9] M. Kamaya: Fatigue properties of 316 stainless steel and its failure due to internal cracks in low-cycle and extremely low-cycle fatigue regimes, Int. J. Fatigue **32** (2010) 1081–1089.

[10] F. Yoshinaka, T. Sawaguchi, S. Takamori, S. Emura and Y. Inoue: Two-fold improvement of low cycle fatigue resistance of steel by bidirectional transformation-induced plasticity, Int. J. Fatigue **171** (2023) 107581.

[11] J. Su, X. Wu, D. Raabe and Z. Li: Deformation-driven bidirectional transformation promotes bulk nanostructure formation in a metastable interstitial high entropy alloy, Acta Mater. **167** (2019) 23–39.

[12] S.M. Vakili, A. Zarei-Hanzaki, A.S. Anoushe, H.R. Abedi, M.H. Mohammad-Ebrahimi, M. Jaskari, S. Sohn, D. Ponge and L.P. Karjalainen: Reversible dislocation movement, martensitic transformation and nano-twinning during elastic cyclic loading of a metastable high entropy alloy, Acta Mater. **185** (2020) 474–492.

[13] W. Lu, C.H. Liebscher, G. Dehm, D. Raabe and Z. Li: Bidirectional transformation enables hierarchical nanolaminate dual-phase high-entropy alloys, Adv. Mater. **30** (2018) 1804727.

[14] M. Risbet and X. Feaugas: Some comments about fatigue crack initiation in relation to cyclic slip irreversibility, Eng. Fract. Mech. **75** (2008) 3511–3519.

[15] H. Mughrabi: Cyclic slip irreversibilities and the evolution of fatigue damage, Metall. Mater. Trans. B **40** (2009) 431–453.

[16] C. Tan, Q. Sun, G. Zhang and Y. Zhao: High-cycle fatigue of a titanium alloy: the role of microstructure in slip irreversibility and crack initiation, J. Mater. Sci. **55** (2020) 12476–12487.

[17] F. Yoshinaka and T. Sawaguchi: Characterization of crystallographic fracture surfaces in Fe–33Mn–6Si alloy, Int. J. Fatigue **130** (2020) 105271.

[18] S. Allain, J.-P. Chateau, O. Bouaziz, S. Migot and N. Guelton: Correlations between the calculated stacking fault energy and the plasticity mechanisms in Fe–Mn–C alloys, Mater. Sci. Eng. A **387–389** (2004) 158–162.

[19] T. Sawaguchi, I. Nikulin, K. Ogawa, S. Takamori, F. Yoshinaka, Y. Chiba, H. Otsuka, Y. Inoue and A. Kushibe: Low-cycle fatigue life and plasticity mechanisms of a Fe–15Mn–10Cr–8Ni–4Si seismic damping alloy under cyclic loading at various temperatures, Acta Mater. **220** (2021) 117267.

[20] I. Nikulin, T. Sawaguchi and K. Tsuzaki: Effect of alloying composition on low-cycle fatigue properties and microstructure of Fe-30Mn-(6-*x*)Si-*x*Al TRIP/TWIP alloys, Mater. Sci. Eng. A **587** (2013) 192–200.

[21] T. Sawaguchi, Y. Tomota, F. Yoshinaka and S. Harjo: Evidence supporting reversible martensitic transformation under cyclic loading on Fe–Mn–Si–Al alloys using in situ neutron diffraction, Acta Mater. **242** (2023) 118494.

[22] J. Komotori and M. Shimizu: Microstructural effect controlling exhaustion of ductility in extremely low-cycle fatigue, Trans. Jpn. Soc. Mech. Eng. Ser. A **57** (1991) 2879–2883.

[23] M. Koyama, T. Sawaguchi and K. Tsuzaki: Premature fracture mechanism in an Fe-Mn-C austenitic steel, Metall. Mater. Trans. A **43** (2012) 4063–4074.

[24] A.T. Zehnder and A.J. Rosakis: Experimental measurement of the temperature rise generated during dynamic crack growth in metals, Appl. Mech. Rev. **43** (1990) S260–S265.